

Molecular dynamics with quantum transitions for proton transfer: Quantum treatment of hydrogen and donor–acceptor motions

Soo Young Kim and Sharon Hammes-Schiffer

Department of Chemistry, Pennsylvania State University, University Park, Pennsylvania 16802

(Received 2 May 2003; accepted 27 May 2003)

The mixed quantum/classical molecular dynamics with quantum transitions (MDQT) method is extended to treat the donor–acceptor vibrational motion as well as the hydrogen motion quantum mechanically for proton transfer reactions. The quantum treatment of both the hydrogen and the donor–acceptor motions requires the calculation of two-dimensional vibrational wave functions. The MDQT surface hopping method incorporates nonadiabatic transitions among these adiabatic vibrational states. This approach is applied to a model representing intramolecular proton transfer within a phenol-amine complex in liquid methyl chloride. For this model, the rates and kinetic isotope effects are the same within statistical uncertainty for simulations in which only the hydrogen motion is treated quantum mechanically and simulations in which both the hydrogen and the donor–acceptor vibrational motions are treated quantum mechanically. The analysis of these simulations elucidates the fundamental issues arising from a quantum mechanical treatment of the donor–acceptor vibrational motion as well as the hydrogen motion. This insight is relevant to future mixed quantum/classical molecular dynamics simulations of proton and hydride transfer reactions in solution and in enzymes. © 2003 American Institute of Physics. [DOI: 10.1063/1.1592509]

I. INTRODUCTION

Proton transfer reactions are ubiquitous throughout chemistry and biology. The computer simulation of proton transfer reactions in condensed phases is challenging due to the importance of nuclear quantum effects.^{1,2} Numerous methods have been developed to address this challenge.^{3–28} One successful approach for studying proton transfer in condensed phases is mixed quantum/classical molecular dynamics, where one or a few nuclei are treated quantum mechanically while the remaining nuclei are treated classically. In the adiabatic mixed quantum/classical method,^{15,28} the system remains in a single adiabatic vibrational state. This paper centers on the molecular dynamics with quantum transitions (MDQT) surface hopping method,^{19,29} which incorporates nonadiabatic transitions among the vibrational states. The MDQT method has been applied to hydrogen transfer in solution¹⁹ and in enzymes.^{27,30–32}

The model system studied in this paper is the intramolecular reaction $AH-B \rightleftharpoons A^- - {}^+HB$ in liquid methyl chloride, where AHB represents a phenol-amine complex.⁷ In the gas phase, the ionic product is much higher in energy than the covalent reactant. As illustrated in Fig. 1, however, the dipolar solvent can stabilize the ionic product via electrostatic solute–solvent interactions. Thus, the reorganization of the solvent plays an important role in this proton transfer reaction. In addition, the nuclear quantum effects of the transferring hydrogen, including zero point motion, energy quantization, and tunneling, are significant for this system.

This model system has been investigated with a variety of methods. It was initially constructed and studied by Azzouz and Borgis with a Landau–Zener curve-crossing approach and a path-integral centroid approach.^{7,33} Subsequently, it was studied with the MDQT mixed quantum/

classical surface hopping approach.¹⁹ In this implementation of MDQT, the transferring hydrogen nucleus was treated quantum mechanically, while the donor, acceptor, and solvent were treated classically. More recently, this model has been investigated by Antoniou and Schwartz^{34,35} with a flux correlation function formalism and by McRae and co-workers³⁶ with semiclassical variational transition state theory. The various methods resulted in a wide range of calculated rate constants and deuterium kinetic isotope effects.

In this paper, we present the methodology for treating both the hydrogen and the donor–acceptor vibrational motions quantum mechanically within the framework of MDQT. The translational and rotational degrees of freedom for the hydrogen-bonded complex and all solvent degrees of freedom are treated classically. We apply this method to the model proton transfer reaction $AH-B \rightleftharpoons A^- - {}^+HB$ in liquid methyl chloride for a linear AHB complex.⁷ The treatment of only the hydrogen motion quantum mechanically requires the calculation of a one-dimensional wave function, whereas the treatment of both the hydrogen and the donor–acceptor vibrational motions quantum mechanically requires the calculation of a two-dimensional wave function. We denote the former treatment as a 1D and the latter treatment as a 2D mixed quantum/classical approach. The 2D MDQT method is shown to be computationally tractable for the simulation of proton transfer in solution. We present the rate constants and kinetic isotope effects obtained with 1D and 2D adiabatic and nonadiabatic quantum/classical methods.

The calculated rates and kinetic isotope effects may be compared to previous results from alternative computational methods.^{7,19,33–36} Unfortunately, a definitive benchmark is not available for this system. The calculated results cannot be compared to experiment because the proton transfer model

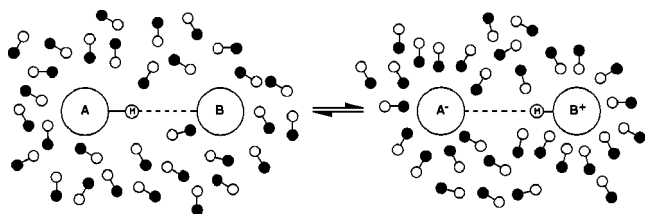


FIG. 1. Schematic picture of the intramolecular proton transfer reaction in liquid methyl chloride. The filled circles indicate the positive ends and the open circles indicate the negative ends of the solvent dipoles. The equilibrium solvent configurations are qualitatively different for the reactant and product solute complexes. The dipolar solvent is randomly oriented around the covalent reactant but is oriented in a manner to stabilize the ionic product via electrostatic interactions.

was not chosen to represent a particular experimental system. Moreover, an exact fully quantum calculation is not computationally feasible for this large system. Thus, we focus on a comparison between 1D and 2D MDQT to elucidate the fundamental issues arising from a quantum mechanical treatment of the donor–acceptor vibrational motion as well as the hydrogen motion. The general physical principles will be applicable to a wide range of proton transfer systems.

II. METHODS

A. Fundamental aspects of mixed quantum/classical methods

In mixed quantum/classical (Q/C) methods,^{20,21} the system is divided into a classical subsystem with coordinates $\mathbf{R}_{\text{class}}$ and a quantum subsystem with coordinates $\mathbf{R}_{\text{quant}}$. The quantum mechanical Hamiltonian H_{quant} is a sum of the kinetic energy of the quantum subsystem and the total potential energy, which depends on $\mathbf{R}_{\text{class}}$ and $\mathbf{R}_{\text{quant}}$. The adiabatic states $\Phi_n(\mathbf{R}_{\text{quant}}; \mathbf{R}_{\text{class}})$ are calculated at each classical molecular dynamics time step by solving the time-independent Schrödinger equation,

$$H_{\text{quant}}\Phi_n(\mathbf{R}_{\text{quant}}; \mathbf{R}_{\text{class}}) = \varepsilon_n(\mathbf{R}_{\text{class}})\Phi_n(\mathbf{R}_{\text{quant}}; \mathbf{R}_{\text{class}}). \quad (1)$$

In the adiabatic approach, the classical coordinates move on a single adiabatic potential energy surface $\varepsilon_k(\mathbf{R}_{\text{class}})$, where k represents the occupied adiabatic state. The Hellmann–Feynman forces,

$$\mathbf{F}_{\mathbf{R}_{\text{class}}}^{\text{HF}} = -\langle \Phi_k | \nabla_{\mathbf{R}_{\text{class}}} H_{\text{quant}} | \Phi_k \rangle \quad (2)$$

are used to numerically integrate the classical equations of motion. (Here the angular brackets indicate integration over all quantum coordinates.)

The molecular dynamics with quantum transitions (MDQT) method^{19,29} incorporates nonadiabatic effects. The fundamental principle of MDQT is that an ensemble of trajectories is propagated, and each trajectory moves classically on a single adiabatic surface except for instantaneous transitions among the adiabatic states. The classical subsystem evolves according to the adiabatic potential $\varepsilon_k(\mathbf{R}_{\text{class}})$ with forces $\mathbf{F}_{\mathbf{R}_{\text{class}}}^{\text{HF}}$, where k denotes the occupied state. The time-dependent wave function describing the quantum nuclei is expanded in a basis of the adiabatic states,

$$\Psi(\mathbf{R}_{\text{quant}}, \mathbf{R}_{\text{class}}, t) = \sum_j C_j(t) \Phi_j(\mathbf{R}_{\text{quant}}; \mathbf{R}_{\text{class}}). \quad (3)$$

The quantum amplitudes $C_j(t)$ are calculated by integrating the time-dependent Schrödinger equation simultaneously with the classical equations of motion. Substituting Eq. (3) into the time-dependent Schrödinger equation leads to

$$i\hbar \dot{C}_n = \sum_j C_j (V_{nj} - i\hbar \dot{\mathbf{R}}_{\text{class}} \cdot \mathbf{d}_{nj}), \quad (4)$$

where

$$V_{nj} \equiv \langle \Phi_n | H_{\text{quant}} | \Phi_j \rangle, \quad (5)$$

$$\mathbf{d}_{nj} \equiv \langle \Phi_n | \nabla_{\mathbf{R}_{\text{class}}} \Phi_j \rangle. \quad (6)$$

At each time step, Tully's “fewest switches” algorithm²⁹ is invoked to determine if a quantum transition to another adiabatic state should occur. This algorithm correctly apportions trajectories among the adiabatic states according to the quantum probabilities $|C_j(t)|^2$ with the minimum required number of quantum transitions (neglecting difficulties with classically forbidden transitions). According to Eq. (4), the quantum amplitudes change most rapidly in the region of large nonadiabatic coupling $\dot{\mathbf{R}}_{\text{class}} \cdot \mathbf{d}_{nj}$. As a result, the nonadiabatic transitions occur most frequently in this coupling region. The MDQT method has been shown to agree with fully quantum dynamical calculations for simple model proton transfer systems.^{37–39}

B. Mixed quantum/classical dynamics with two quantum coordinates

In this section, we present the methodology for treating both the transferring hydrogen and the donor–acceptor vibrational motions quantum mechanically in mixed Q/C molecular dynamics simulations involving proton transfer within a linear AHB complex embedded in solvent. The solvent coordinates are represented as \mathbf{R}_S . The linear complex may be described in terms of the coordinates \mathbf{R}_A , \mathbf{R}_B , and \mathbf{R}_H corresponding to the positions of A, B, and H, respectively, where H is constrained to be on the AB axis. Alternatively, the linear complex may be described in terms of the center of mass \mathbf{R}_{cm} , the polar coordinates (θ, ϕ) representing the orientation, and the scalar distances $r = |\mathbf{R}_A - \mathbf{R}_H|$ and $R = |\mathbf{R}_B - \mathbf{R}_A|$. The masses of A, B, and H are represented by m_A , m_B , and m_H , respectively, and the total mass is $M = m_A + m_B + m_H$.

Within this framework, the total Hamiltonian is³⁶

$$H = T_{\text{solv}}(\mathbf{P}_S) + \frac{\mathbf{P}_{\text{cm}}^2}{2M} + \frac{1}{2I} \left(P_\theta^2 + \frac{P_\phi^2}{\sin^2 \theta} \right) + \frac{1}{2} (P_r, P_R) \boldsymbol{\mu}^{-1} \begin{pmatrix} P_r \\ P_R \end{pmatrix} + V(r, R, \mathbf{R}_{\text{cm}}, \theta, \phi, \mathbf{R}_S), \quad (7)$$

where the first four terms correspond to the kinetic energies of the solvent, the center of mass of the complex, the angles representing the orientation of the complex, and the scalar coordinates r and R . The last term represents the potential energy of the system. The effective mass matrix and its inverse are³⁶

$$\boldsymbol{\mu} = \frac{1}{M} \begin{pmatrix} (m_A + m_B)m_H & -m_H m_B \\ -m_H m_B & (m_A + m_H)m_B \end{pmatrix} \quad (8)$$

$$\boldsymbol{\mu}^{-1} = \begin{pmatrix} \frac{1}{\mu_{AH}} & \frac{1}{m_A} \\ \frac{1}{m_A} & \frac{1}{\mu_{AB}} \end{pmatrix},$$

where $\mu_{AH} = m_A m_H / (m_A + m_H)$ and $\mu_{AB} = m_A m_B / (m_A + m_B)$. The moment of inertia along the axis of the linear complex is³⁶

$$I = (r, R) \boldsymbol{\mu} \begin{pmatrix} r \\ R \end{pmatrix} = \frac{1}{M} [(m_A + m_B)m_H r^2 - 2m_H m_B R r + (m_A + m_H)m_B R^2]. \quad (9)$$

The conjugate momenta are defined in terms of the time derivatives of the coordinates as

$$\mathbf{P}_{\text{cm}} = M \dot{\mathbf{R}}_{\text{cm}}, \quad P_\theta = I \dot{\theta}, \quad P_\phi = I \sin^2 \theta \dot{\phi},$$

and

$$\begin{pmatrix} P_r \\ P_R \end{pmatrix} = \boldsymbol{\mu} \begin{pmatrix} \dot{r} \\ \dot{R} \end{pmatrix}.$$

In the 2D Q/C method, we treat the coordinates r and R quantum mechanically and all other coordinates classically. The kinetic energy corresponding to the quantum coordinates r and R can be expressed as

$$\frac{1}{2} (P_r, P_R) \boldsymbol{\mu}^{-1} \begin{pmatrix} P_r \\ P_R \end{pmatrix} = -\frac{\hbar^2}{2} \left(\frac{1}{\mu_{AH}} \frac{\partial^2}{\partial r^2} + \frac{2}{m_A} \frac{\partial^2}{\partial r \partial R} + \frac{1}{\mu_{AB}} \frac{\partial^2}{\partial R^2} \right). \quad (10)$$

Equations (7) and (9) indicate that the r and R coordinates are not rigorously separable from the other coordinates in the Hamiltonian due to the dependence of I on r and R . For the 2D Q/C approach, however, we define the quantum mechanical Hamiltonian as

$$H_{\text{quant}}^{2D} = -\frac{\hbar^2}{2} \left(\frac{1}{\mu_{AH}} \frac{\partial^2}{\partial r^2} + \frac{2}{m_A} \frac{\partial^2}{\partial r \partial R} + \frac{1}{\mu_{AB}} \frac{\partial^2}{\partial R^2} \right) + V(r, R, \mathbf{R}_{\text{cm}}, \theta, \phi, \mathbf{R}_S). \quad (11)$$

The time-independent Schrödinger equation for fixed classical coordinates is

$$H_{\text{quant}}^{2D} \Phi_n(r, R; \mathbf{R}_{\text{cm}}, \theta, \phi, \mathbf{R}_S) = \varepsilon_n(\mathbf{R}_{\text{cm}}, \theta, \phi, \mathbf{R}_S) \Phi_n(r, R; \mathbf{R}_{\text{cm}}, \theta, \phi, \mathbf{R}_S). \quad (12)$$

For each classical configuration obtained during the molecular dynamics simulation, we solve this Schrödinger equation numerically on a two-dimensional grid using a Fourier grid Hamiltonian method.^{40,41} The R -grid is generated by moving A and B along the AB axis while maintaining the same orientation (θ, ϕ) and the same center of mass \mathbf{R}_{cm} (neglecting the mass of H). The r -grid is generated by moving H along

the AB axis with an origin of \mathbf{R}_A . The classical coordinates are propagated according to the classical equations of motion with potential energy $\varepsilon_k(\mathbf{R}_{\text{cm}}, \theta, \phi, \mathbf{R}_S)$, where k denotes the occupied adiabatic state. We treat the linear complex as a rigid rotor of length $\langle R \rangle_k = \langle \Phi_k | R | \Phi_k \rangle$, where the angular brackets indicate integration over r and R . In practice, the five classical coordinates are propagated as \mathbf{R}_A and \mathbf{R}_B with the constraint $|\mathbf{R}_B - \mathbf{R}_A| = \langle R \rangle_k$ rather than as $\mathbf{R}_{\text{cm}}, \theta, \phi$.

In the 1D Q/C method,¹⁹ only the H coordinate r is treated quantum mechanically. In this case, the coupling term between r and R in the kinetic energy is neglected and $\mu_{AH} \approx m_H$. The 1D quantum mechanical Hamiltonian is

$$H_{\text{quant}}^{1D} = -\frac{\hbar^2}{2m_H} \frac{\partial^2}{\partial r^2} + V(r, R, \mathbf{R}_{\text{cm}}, \theta, \phi, \mathbf{R}_S), \quad (13)$$

leading to the following time-independent Schrödinger equation for fixed classical coordinates:

$$H_{\text{quant}}^{1D} \Phi_n(r; R, \mathbf{R}_{\text{cm}}, \theta, \phi, \mathbf{R}_S) = \varepsilon_n(R, \mathbf{R}_{\text{cm}}, \theta, \phi, \mathbf{R}_S) \Phi_n(r; R, \mathbf{R}_{\text{cm}}, \theta, \phi, \mathbf{R}_S). \quad (14)$$

For each classical configuration, this equation is solved numerically on a one-dimensional grid generated by moving H along the AB axis with an origin of \mathbf{R}_A . The classical coordinates are propagated according to the classical equations of motion with potential energy $\varepsilon_k(R, \mathbf{R}_{\text{cm}}, \theta, \phi, \mathbf{R}_S)$. In practice, the six classical coordinates are propagated as \mathbf{R}_A and \mathbf{R}_B rather than as $R, \mathbf{R}_{\text{cm}}, \theta, \phi$.

The main approximation in both the 1D and 2D Q/C methods is the treatment of only one or two degrees of freedom quantum mechanically. Not only is the solvent treated differently from the AHB complex, but a separation of coordinates occurs within the linear AHB complex. In the 1D Q/C method, the vibrational degree of freedom r is separated from the other vibrational degree of freedom R , as well as the rotational degrees of freedom of the complex. In the 2D Q/C method, the vibrational degrees of freedom r and R are separated from the rotational degrees of freedom of the complex. Both treatments also neglect the mass of H relative to A and B (i.e., assume that $m_H \ll m_A, m_B$).

C. Model proton transfer system

The model system studied in this paper is essentially the same as that used by Azzouz and Borgis⁷ and subsequently by Hammes-Schiffer and Tully.¹⁹ The proton transfer reaction is $\text{AH} - \text{B} \rightleftharpoons \text{A}^- - {}^+\text{HB}$ in liquid methyl chloride, where AHB is a linear complex with parameters chosen to model a phenol-amine complex (i.e., A and B represent a phenolate anion and trimethyl amine, respectively). The simulation system includes one hydrogen-bonded AHB complex and 255 methyl chloride molecules placed in a periodically replicated cube, where a side of the cube has a length of 28 Å. The AHB complex consists of three sites: the phenolate donor (A), the trimethyl amine acceptor (B), and the transferring proton (H). Each solvent molecule consists of two sites, a methyl group and a chloride atom, and is treated as a rigid rotor with a fixed distance of 1.781 Å. The simulations were performed at 247 K.

The gas phase potential energy within the AHB complex is given by

$$V_{\text{HB}}(r, R) = b \exp(-aR) + D_A \left[1 - \exp\left(\frac{-n_A(r-d_A)^2}{2r}\right) \right] + cD_A \left[1 - \exp\left(\frac{-n_B(R-r-d_B)^2}{2(R-r)}\right) \right]. \quad (15)$$

All parameters for this potential are given in Ref. 19. The masses of A and B are $m_A = 93$ amu and $m_B = 59$ amu, which correspond to the masses of phenolate and trimethylamine, respectively.

The complex-solvent and solvent-solvent interactions consist of Lennard-Jones and Coulombic potentials. The charges on the solvent molecule sites are fixed, but the charges on the complex sites depend on the position r of the H atom. These r -dependent charges $e_\alpha(r)$ are of the form,

$$e_\alpha(r) = [1 - f(r)]e_\alpha^c + f(r)e_\alpha^i, \quad \alpha = \text{A, H, B},$$

$$f(r) = \frac{1}{2} \left[1 + \frac{r - r_o}{\sqrt{(r - r_o)^2 + l^2}} \right]. \quad (16)$$

All parameters for the Lennard-Jones and Coulombic potentials are given in Ref. 19. The Lennard-Jones potential for the solvent-solvent and solvent-complex interactions was spherically truncated at $R_c = 13.8$ Å and shifted accordingly. The Coulombic potential for the solvent-solvent and solvent-complex interactions was smoothly truncated to zero at $R_c = 13.8$ Å as described in Ref. 19.

D. Simulation details

This section provides the details of the calculations. Previously the same model system was studied with a mixed 1D Q/C method in which only the proton coordinate r was treated quantum mechanically.¹⁹ This paper presents results from the 1D Q/C method with slightly modified methodology, as well as results from the new 2D Q/C method. For comparison, we point out the differences between the previous and the current methodologies.

The time-independent Schrödinger equations were solved using a Fourier grid Hamiltonian (FGH) method.^{40,41} In the FGH method, the basis functions are delta functions with equal spacing in the coordinate representation. For the 1D Q/C Schrödinger equation [Eq. (14)], a one-dimensional grid representing the proton coordinate r was formed along the AB axis with the origin at \mathbf{R}_A . This grid consisted of 64 equally spaced points spanning the range $0.4 \text{ Å} \leq r \leq 2.4 \text{ Å}$. For the 2D Q/C Schrödinger equation [Eq. (12)], a two-dimensional grid representing the proton coordinate r and the AB vibrational coordinate R was formed. The r -grid was formed along the AB axis with the origin at \mathbf{R}_A , and the R -grid was formed by moving A and B along the AB axis while maintaining the same center of mass (neglecting the mass of H). The r -grid consisted of 32 equally spaced points spanning the range $0.4 \text{ Å} \leq r \leq 2.9 \text{ Å}$, and the R -grid consisted of 32 equally spaced points spanning the range 2.4 Å

$\leq R \leq 3.3 \text{ Å}$. The Davidson method⁴² was used to diagonalize the Hamiltonian matrix for the two-dimensional basis function grid.

Note that the previous 1D Q/C calculations for this system¹⁹ did not utilize the FGH method. These previous 1D MDQT calculations used basis functions of the form of the solutions for a quantum mechanical simple harmonic oscillator. The use of harmonic oscillator basis functions is computationally expensive due to numerical integration of the potential energy matrix and introduces bias from the choice of the centers and frequencies of the basis functions. In contrast, numerical integration is not needed for the FGH method, and no bias is introduced from the equally spaced grid points in the FGH method. The disadvantage of the FGH method is that the number of basis functions required to construct accurate wave functions is often relatively large. This disadvantage was not problematic for the calculations presented in this paper.

The classical equations of motion were integrated with the RATTLE algorithm,⁴³ which is based on the velocity Verlet algorithm and allows the constraint of intramolecular bond lengths. For the adiabatic simulations, the classical time step was 1.0 fs. For the nonadiabatic simulations, the classical time step was decreased to 0.1 fs in the coupling region. Specifically, if $\langle \Phi_0(t) | r | \Phi_0(t) \rangle > 1.10 \text{ Å}$ and the time step was still 1.0 fs, the trajectory was returned to the previous time step, and the value of the time step was decreased to 0.1 fs. The time step was increased to 1.0 fs when the trajectory left the coupling region and returned to the reactant region [i.e., if $\langle \Phi_0(t) | r | \Phi_0(t) \rangle < 1.05 \text{ Å}$ after at least twelve steps with the smaller time step]. The trajectory was terminated after it became stabilized in the product region. We found that the time step must be decreased in the coupling region to accurately calculate the nonadiabatic couplings for integration of the time-dependent Schrödinger equation.

The time-dependent Schrödinger equation [Eq. (4)] was propagated with the fourth-order Runge-Kutta numerical integration method⁴⁴ using a time step of 0.001 fs. The nonadiabatic coupling $\hat{\mathbf{R}} \cdot \mathbf{d}_{nj}$ was determined by explicitly calculating the nonadiabatic coupling vector \mathbf{d}_{nj} using the off-diagonal Hellmann-Feynman expression,

$$\mathbf{d}_{nj} = \frac{\langle \Phi_n | \nabla_{\mathbf{R}_{\text{class}}} H_{\text{quant}} | \Phi_j \rangle}{\epsilon_j - \epsilon_n}. \quad (17)$$

For computational efficiency, in the previous 1D Q/C calculations we calculated the nonadiabatic coupling numerically with a finite difference method.¹⁹ The increase in computer power over the past decade has allowed us to avoid this approximation in the current calculations. To eliminate nonphysical coherence in the coefficients, we set the magnitude of the coefficient of the current state k to unity and the magnitude of all other coefficients to zero when the system left the coupling region and entered either the reactant or the product region [i.e., when $\langle \Phi_k(t) | r | \Phi_k(t) \rangle < 1.05 \text{ Å}$ or $\langle \Phi_k(t-\Delta) | r | \Phi_k(t-\Delta) \rangle < 1.62 \text{ Å}$ or $\langle \Phi_k(t-\Delta) | r | \Phi_k(t) \rangle < 1.62 \text{ Å}$].

The fewest switches surface hopping method was implemented as described in Ref. 19, with the exception of the velocity adjustment after a nonadiabatic transition. Previously the velocities were reversed along the component of the nonadiabatic coupling vector after classically forbidden nonadiabatic transitions.¹⁹ Recent studies indicate that surface hopping calculations may be more stable without this velocity reversal.^{45,46} Therefore, the 1D MDQT calculations were performed both with and without the velocity reversal, while the 2D MDQT calculations were performed only without the velocity reversal. As will be shown below, the method of velocity adjustment does not significantly influence the results for this model system. The four lowest energy vibrational states were included for both the 1D and 2D MDQT calculations.

E. Calculating rate constants

In this subsection, we discuss how we calculated rate constants for the proton transfer reaction. A reactive event is defined to occur if the system starts as a reactant and becomes a product. The system is defined to be a reactant if the classical coordinates are reactant stabilizing and is defined to be a product if the classical coordinates are product stabilizing. The classical coordinates are determined to be reactant or product stabilizing based on the value of $\langle r \rangle_0 \equiv \langle \Phi_0 | r | \Phi_0 \rangle$, where the angular brackets indicate integration over the quantum coordinate(s) (i.e., r for 1D Q/C and r and R for 2D Q/C). For the purposes of defining a reactive event, the system is reactant stabilizing if $\langle r \rangle_0 < 1.05$ Å and product stabilizing if $\langle r \rangle_0 > 1.62$ Å. For the 1D Q/C method, the system must be in the vibrational ground state to be considered a reactant or product. For the 2D Q/C method, the system may be in an excited vibrational state because the lowest three excited vibrational states correspond to the ground state hydrogen vibrational mode (i.e., excited donor–acceptor vibrational modes) in the reactant and product regions.

To obtain initial conditions, we generated a set of ground state configurations for the classical coordinates and momenta in the reactant stabilizing region. These configurations were generated after 100 ps of classical equilibration, followed by 10 ps of either 1D or 2D Q/C adiabatic equilibration at 247 K. After this equilibration, the adiabatic simulations were continued, and 20 configurations were generated by viewing configurations every 10 ps and accepting only those configurations in the reactant region. From these configurations we could generate different microcanonical trajectories by producing a random Gaussian distribution of velocities with an approximate temperature of 247 K, and then scaling the velocities to have the same kinetic energy as that associated with the original velocities. For the 1D Q/C calculations, all trajectories were started in the ground state since the Boltzmann population of the first excited vibrational state was determined to be negligible. For the 2D Q/C calculations, the initial vibrational state was determined stochastically according to the Boltzmann distribution at 247 K. The splitting of the donor–acceptor vibrational mode in the gas phase was determined to be 354 cm^{-1} , which indicates an average population of $\approx 13\%$ in the first excited state and

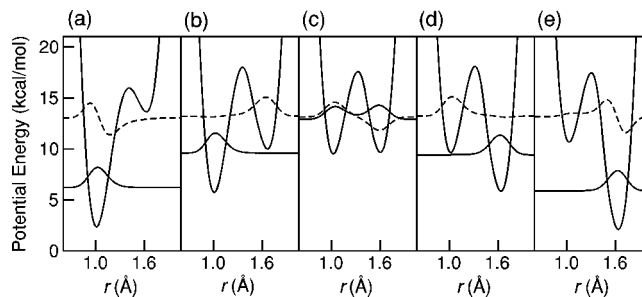


FIG. 2. Representative one-dimensional hydrogen potential energy curves in r , as well as the associated hydrogen vibrational wave functions, for five different solvent configurations corresponding to the (a) reactant with the lowest two vibrational states localized in the same well, (b) reactant with the lowest two vibrational states localized in different wells, (c) intermediate, (d) product with the lowest two vibrational states localized in different wells, and (e) product with the lowest two vibrational states localized in the same well. The ground state wave function is solid, and the first excited state wave function is dashed. The relative energies among the five curves and the magnitudes of the wave functions are arbitrary.

$\approx 2\%$ in the second excited state. The system was equilibrated in the ground vibrational state since the solvent configurations are not influenced significantly by excited donor–acceptor vibrational states.

We propagated 200 reactive trajectories for each type of simulation. The trajectories were terminated when the solvent was determined to be product-stabilizing as defined above. The rate constant was calculated by adding up the number of reactive events for the trajectories and dividing this by the total time for all trajectories. We repeated this procedure replacing the hydrogen with deuterium to calculate the kinetic isotope effect.

III. RESULTS

We investigate both hydrogen and deuterium transfer with the 1D and 2D adiabatic and MDQT approaches. The rates are calculated for each type of simulation. Our analysis focuses on the differences between the 1D and 2D quantum mechanical treatments. For this purpose, we examine the potential energy curves and the associated vibrational wave functions for various solvent configurations. In addition, we compare average properties, such as nonadiabatic couplings, quantum amplitudes, energy splittings, and numbers of nonadiabatic transitions, for the 1D and 2D MDQT methods. This analysis elucidates the fundamental physical principles underlying the 2D MDQT approach.

Figure 2 depicts representative one-dimensional hydrogen potential energy curves and the associated hydrogen vibrational wave functions for five different solvent configurations. The electrostatic interactions between the solvent and the solute lead to qualitative changes in the shape of the hydrogen potential energy curve as the solvent fluctuates. Figure 1 illustrates the reactant-stabilizing and product-stabilizing solvent configurations. In the reactant-stabilizing solvent configurations, the reactant well is lower in energy and the ground vibrational state is localized in the reactant well, as shown in Figs. 2(a) and 2(b). In Fig. 2(a) the reactant well is so much lower in energy that both the ground and first excited vibrational states are localized in the reactant well,

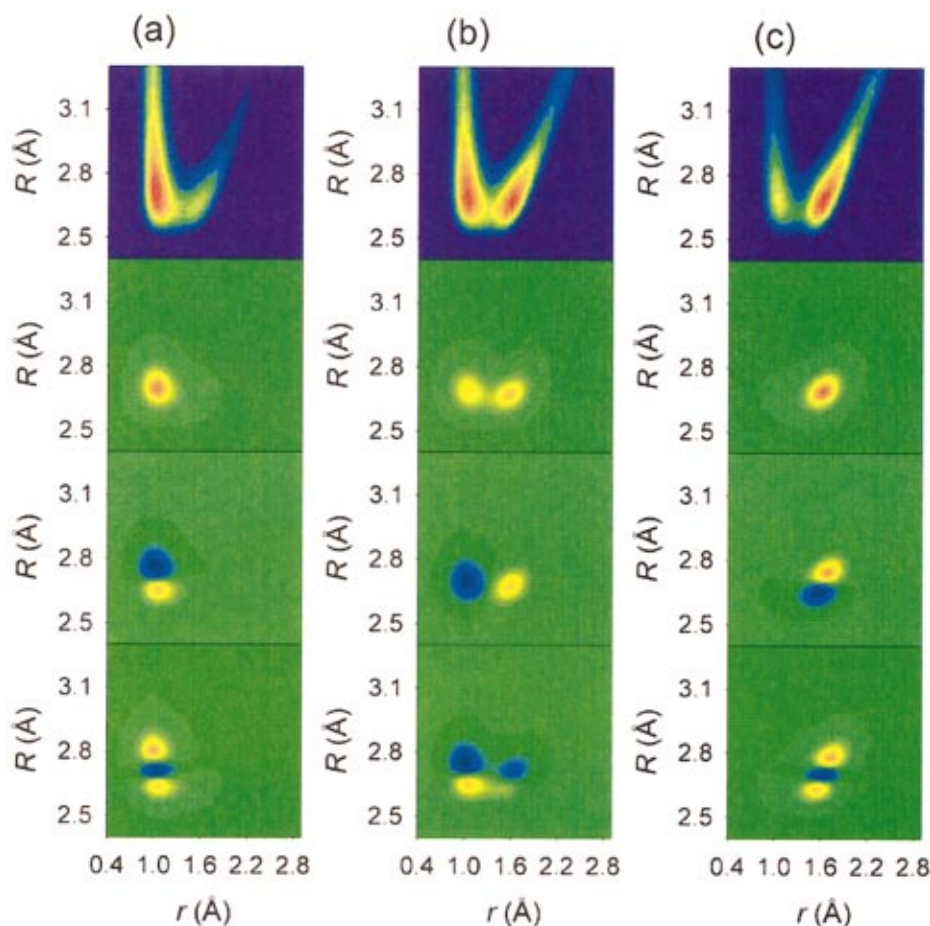


FIG. 3. (Color) Representative two-dimensional potential energy surfaces in r and R , as well as the corresponding two-dimensional wave functions, for three different solvent configurations corresponding to the (a) reactant, (b) intermediate, and (c) product. For each solvent configuration, the potential energy surface is given at the top, followed by the three lowest energy vibrational wave functions in order of increasing energy. Note that the excited vibrational states correspond to excitations of the donor-acceptor vibrational mode for the reactant and product, whereas the first excited vibrational state corresponds to excitation of the hydrogen vibrational mode for the intermediate.

whereas in Fig. 2(b) the first excited vibrational state is localized in the product well. In the product-stabilizing configurations, the product well is lower in energy and the ground vibrational state is localized in the product well, as shown in Figs. 2(d) and 2(e). As the reaction evolves from the reactant to the product, the solvent acquires a configuration associated with a nearly symmetric double well potential in which the ground and first excited vibrational states are delocalized over the two wells, as shown in Fig. 2(c). As discussed above, the nonadiabatic transitions tend to occur in this strong coupling region.

For comparison, Fig. 3 depicts representative two-dimensional potential energy surfaces in r and R , as well as the corresponding two-dimensional wave functions. In the reactant-stabilizing solvent configuration [Fig. 3(a)], the ground and lowest two excited vibrational states are localized in the reactant well along the r -axis. For this solvent configuration, the lowest two excited vibrational states correspond to excitations of the donor-acceptor vibrational mode along the R -axis. The product-stabilizing solvent configuration [Fig. 3(c)] is similar except the ground and lowest two excited vibrational states are localized in the product well along the r -axis. In contrast, for the intermediate solvent configuration [Fig. 3(b)], the ground and first excited vibrational states are delocalized over the reactant and product wells along the r -axis and correspond to the ground (symmetric) and first excited (antisymmetric) vibrational states in Fig. 2(c). For this solvent configuration, the first excited vi-

brational state corresponds to excitation of the hydrogen vibrational mode along the r -axis. Thus, the first excited vibrational state wave function changes character in the coupling region. The second excited vibrational state corresponds to a mixture of excitations of the hydrogen and donor-acceptor vibrational modes in the coupling region.

We also compare trajectories generated with the 1D and 2D MDQT methods. Figure 4 depicts the time evolution of the donor-acceptor distance, the nonadiabatic coupling, the energies, and the hydrogen position for representative 1D and 2D MDQT trajectories. For the 1D MDQT method, the donor-acceptor distance R oscillates significantly between 2.65 and 2.73 Å, whereas for the 2D MDQT method, $\langle R \rangle_k$ does not oscillate because it represents an average value. The coupling region occurs at 421 fs $< t < 446$ fs for the 1D MDQT trajectory and at 580 fs $< t < 625$ fs for the 2D MDQT trajectory. The nonadiabatic coupling exhibits a peak in the coupling region. Note that the donor-acceptor distance decreases in the coupling region for both the 1D and 2D MDQT trajectories. Outside of the coupling region, the energy splitting between the lowest two vibrational states is smaller for 2D than for 1D MDQT, as expected because the donor-acceptor vibrational mode frequency is lower than the hydrogen vibrational mode frequency. (Based on the splittings of the gas phase vibrational states, the donor-acceptor vibrational mode frequency is 354 cm⁻¹, and the hydrogen vibrational mode frequency is 2384 cm⁻¹.) Moreover, outside of the coupling region, the energy splitting remains rela-

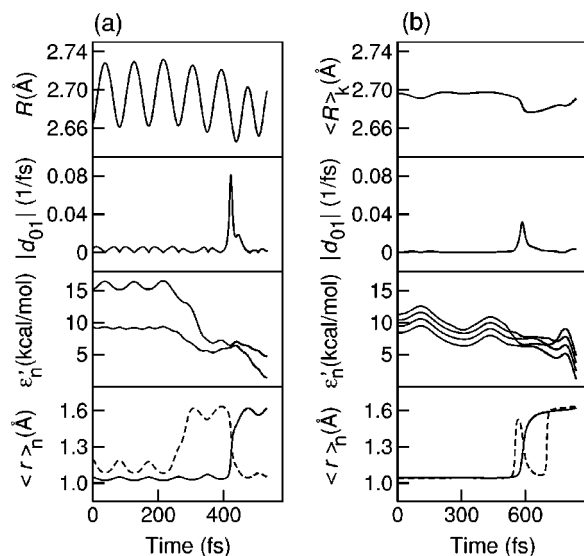


FIG. 4. Time evolution of relevant properties for representative trajectories calculated with the (a) 1D MDQT and (b) 2D MDQT methods. The top panels depict R for 1D MDQT and $\langle R \rangle_k$ for 2D MDQT, where k denotes the occupied adiabatic vibrational state. The panels second from the top depict the absolute value of the nonadiabatic coupling $|d_{01}| = |\dot{\mathbf{R}}_{\text{class}} \cdot \mathbf{d}_{01}|$. The panels third from the top depict ε_n , where the prime indicates that the solvent-solvent interaction energy is removed from the eigenvalue ε_n for illustrative purposes. The bottom panels depict $\langle r \rangle_0$ (solid) and $\langle r \rangle_1$ (dashed).

tively constant for the 2D MDQT trajectory because the solvent fluctuations do not significantly influence the donor-acceptor vibrational mode, whereas the energy splitting fluctuates considerably for the 1D MDQT trajectory because the hydrogen motion is significantly influenced by the solvent. For both trajectories, the energy splitting decreases in the coupling region.

The 1D MDQT trajectory in Fig. 4(a) illustrates the common characteristics of one-dimensional quantum/classical trajectories. For $t < 215$ fs, the hydrogen potential energy curve resembles Fig. 2(a) (i.e., the reactant well is so much lower than the product well that both the ground and excited vibrational states are localized in the reactant well), as shown by the expectation values of the hydrogen coordinate, where $\langle r \rangle_0 \approx 1.01$ Å and $\langle r \rangle_1 < 1.2$ Å. In this case, the energy splitting is relatively constant (≈ 6.63 kcal/mol $= 2320$ cm $^{-1}$) and is consistent with the gas phase hydrogen vibrational frequency of 2384 cm $^{-1}$. For 309 fs $< t < 393$ fs, the hydrogen potential energy curve resembles Fig. 2(b) (i.e., the ground and excited vibrational states are localized in different wells). In this case, $\langle r \rangle_0 \approx 1.05$ Å and $\langle r \rangle_1 \approx 1.55$ Å, and the energy splitting becomes smaller. In the coupling region (421 fs $< t < 446$ fs), the hydrogen potential energy curve resembles Fig. 2(c), and the energy splitting reaches a minimum value. As the trajectory passes through the coupling region, the expectation values of the hydrogen coordinate for the ground and excited states are interchanged. For $t > 450$ fs, the hydrogen potential energy curve resembles Fig. 2(d), and $\langle r \rangle_0 \approx 1.55$ Å and $\langle r \rangle_1 \approx 1.05$ Å. Typically the trajectories are terminated before reaching the configurations corresponding to the hydrogen potential energy curve in Fig. 2(e).

For comparison, the 2D MDQT trajectory in Fig. 4(b)

TABLE I. Rate constants in units of 10^{11} s $^{-1}$ obtained from simulations using 1D and 2D adiabatic and nonadiabatic methods for hydrogen (H) and deuterium (D). The estimated statistical uncertainty is 15%.

Simulation method	k for H	k for D
1D adiabatic	1.69	1.60
2D adiabatic	1.47	1.42
1D nonadiabatic (reversal)	0.73	0.20
1D nonadiabatic (no reversal)	1.04	0.22
2D nonadiabatic (no reversal)	1.25	0.20

illustrates the common characteristics of two-dimensional quantum/classical trajectories. Outside of the coupling region, the first excited vibrational state corresponds to excitation of the donor-acceptor vibrational mode, which is not significantly influenced by the solvent. As a result, the energy splittings remain nearly constant (≈ 1.05 kcal/mol $= 366$ cm $^{-1}$) and are consistent with the gas phase donor-acceptor vibrational frequency of 354 cm $^{-1}$. For $t < 520$ fs, $\langle r \rangle_1 \approx \langle r \rangle_0 \approx 1.05$ Å [corresponding to Fig. 3(a)], and for $t > 705$ fs, $\langle r \rangle_1 \approx \langle r \rangle_0 \approx 1.55$ Å [corresponding to Fig. 3(c)]. In the coupling region, $\langle r \rangle_1$ fluctuates between the reactant and product values and is different from $\langle r \rangle_0$ because the first excited vibrational state corresponds to excitation of the hydrogen vibrational mode in the coupling region, as shown in Fig. 3(b). This behavior of the expectation values of the hydrogen coordinate illustrates that the first excited vibrational state wave function changes character in the coupling region. Thus, the 1D and 2D MDQT trajectories have similar first excited vibrational states in the coupling region but qualitatively different first excited vibrational states out of the coupling region.

The rates for H and D transfer calculated with the 1D and 2D adiabatic and MDQT methods are given in Table I. The 1D MDQT calculations were performed both with and without the velocity reversal after classically forbidden transitions. The values for the 1D adiabatic and 1D MDQT methods are consistent with the previously calculated results¹⁹ using the same basic approach but a different basis set and an alternative method for calculating the nonadiabatic coupling. As observed previously, the rates are the same for H and D with the adiabatic method because proton transfer occurs whenever the solvent stabilizes the product side so that it is lower in energy than the reactant side, as shown in Fig. 2. (The difference in zero point energies does not appear to significantly affect the dynamics in this case.) The inclusion of nonadiabatic transitions decreases the rate for both H and D transfer. The nonadiabatic rate constant is smaller for deuterium than for hydrogen because tunneling is less probable for deuterium (i.e., the D energy levels are closer together so the probability of a nonadiabatic transition is greater for D than for H). Table I indicates that the elimination of the velocity reversal for classically forbidden transitions slightly increases the rate for H and D transfer, although the differences are within the statistical uncertainties. The most important result in Table I is that the 2D results do not differ substantially from the 1D results. The 2D adiabatic rates for H and D transfer are slightly smaller than the corresponding 1D adiabatic rates, but the differences are within the statisti-

TABLE II. Analysis of 1D and 2D MDQT calculations for H and D transfer. The results are shown only for simulations without velocity reversals after classically forbidden transitions, but the results were found to be insensitive to the method of velocity adjustment. CR denotes the coupling region, defined as $1.15 \text{ \AA} < \langle r \rangle_0 < 1.52 \text{ \AA}$. The nonadiabatic coupling is $d_{01} = \dot{\mathbf{R}}_{\text{class}} \cdot \mathbf{d}_{01}$. The average quantities are calculated for 200 trajectories with each method. The value of the quantum probabilities $|C_0|^2$ are calculated after the trajectories pass through the specified value of $\langle r \rangle_0$ in the forward direction. The root-mean-square deviations are given in parentheses.

Average quantity	1D for H	1D for D	2D for H	2D for D
R or $\langle R \rangle$ in CR (\AA)	2.66 (0.02)	2.66 (0.02)	2.69 (0.01)	2.69 (0.01)
R or $\langle R \rangle$ out of CR (\AA)	2.70 (0.04)	2.70 (0.03)	2.70 (0.01)	2.70 (0.01)
$\varepsilon_1 - \varepsilon_0$ in CR (kcal/mol)	0.5 (0.3)	0.1 (0.1)	0.26 (0.04)	0.034 (0.005)
$\varepsilon_1 - \varepsilon_0$ out of CR (kcal/mol)	5 (2)	4 (1)	1.0 (0.1)	1.0 (0.1)
$ d_{01} $ in CR (1/fs)	0.03 (0.06)	0.3 (0.6)	0.03 (0.02)	0.2 (0.2)
$ d_{01} $ out of CR (1/fs)	0.004 (0.006)	0.003 (0.017)	0.001 (0.002)	0.001 (0.005)
$ C_0 ^2$, $\langle r \rangle_0 = 1.15 \text{ \AA}$	0.8 (0.2)	0.7 (0.2)	0.7 (0.3)	0.7 (0.2)
$ C_0 ^2$, $\langle r \rangle_0 = 1.35 \text{ \AA}$	0.5 (0.1)	0.4 (0.1)	0.5 (0.2)	0.4 (0.1)
No. trans per traj in CR	2.3	11	1.1	8.6
No. trans per traj out of CR	1.2	7.3	1.6	13
No. forb trans per traj in CR	0.8	0.8	0.5	0.5
No. forb trans per traj out of CR	2.6	7.3	1.2	5.3
% time in CR	1.3	0.1	1.0	0.1

cal uncertainties. The 2D nonadiabatic rates for H and D transfer are also the same as the corresponding 1D nonadiabatic rates within the statistical uncertainties.

An analysis of the MDQT data is provided in Table II. We found that the 1D and 2D MDQT trajectories spend the majority of time outside of the coupling region, where the coupling region is defined as $1.15 \text{ \AA} < \langle r \rangle_0 < 1.52 \text{ \AA}$. Specifically, only 1% of the time is spent in the coupling region for H, and only 0.1% of the time is spent in the coupling region for D. Based on the definition of the coupling region, less time is spent in the coupling region for D because the wavefunctions are more localized for D. The values for specified properties both in and out of the coupling region are averaged over 200 trajectories for the 1D and 2D MDQT methods.

Table II quantifies the main differences between the 1D and 2D MDQT trajectories outside of the coupling region. The splitting between the lowest two vibrational states is substantially smaller outside of the coupling region for the 2D simulations than for the 1D simulations. This observation is consistent with Fig. 3(a), which illustrates that the first excited state corresponds to excitation of the donor–acceptor vibrational mode outside of the coupling region for the 2D simulations. This mode has a smaller frequency than the hydrogen vibrational mode and maintains a relatively constant splitting of ≈ 1.0 kcal/mol since this mode is not influenced much by the solvent fluctuations. In contrast, the splitting for the 1D simulations corresponds to excitation of the hydrogen vibrational mode and varies substantially because the first excited vibrational state can be localized in either the same well [Fig. 2(a)] or the opposite well [Fig. 2(b)] as the ground state, depending on the relative energies of the two wells as determined by the solvent configuration. Despite the smaller splitting for the 2D MDQT calculations, the Boltzmann population of the excited 2D vibrational states is still very small ($\approx 15\%$). Moreover, nonadiabatic transitions are unlikely outside of the coupling region for both the 1D and 2D MDQT methods because the nonadiabatic coupling d_{01} is

very small, as also illustrated in Fig. 4. Thus, the differences between the two methods out of the coupling region do not significantly influence the overall rate of proton transfer.

In addition, Table II shows that the 1D and 2D MDQT simulations behave similarly in the coupling region. This observation is consistent with Figs. 2(c) and 3(b), which illustrate that the ground and first excited vibrational states have similar characteristics in the coupling region for the 1D and 2D calculations. In particular, the excitation corresponds to the hydrogen vibrational mode, and the wave functions are symmetric and antisymmetric bilobal wave functions along the r -axis. The average value of the donor–acceptor distance in the coupling region is slightly smaller for the 1D simulations (2.66 \AA) than for the 2D simulations (2.69 \AA), as illustrated in Fig. 4. Consistent with this observation, the average splitting between the lowest two vibrational states in the coupling region is slightly larger for the 1D simulations than for the 2D simulations. These differences, however, are within the statistical uncertainties of the calculations. Moreover, the nonadiabatic transitions in the 1D simulations were found to occur at an average donor–acceptor distance of 2.69 \AA , which is consistent with the corresponding average value for the 2D simulations.

To complete this analysis, Table II indicates that the nonadiabatic couplings are the same for the 1D and 2D simulations both in and out of the coupling region. As a result, the quantum amplitudes evolve similarly for the 1D and 2D simulations. This is verified by the fact that the average quantum probability for the ground vibrational state when $\langle r \rangle_0 = 1.35 \text{ \AA}$ (i.e., in the middle of the coupling region) is the same for the 1D and 2D simulations. The average total number of nonadiabatic transitions is similar for the 1D and 2D MDQT calculations. The slightly smaller number of classically forbidden transitions for the 2D MDQT calculations out of the coupling region is reasonable because the energy splittings are smaller. This difference, however, does not significantly influence the overall rate. Thus, the 1D and 2D rates are virtually indistinguishable for this model system.

IV. SUMMARY AND CONCLUSIONS

The results presented in this paper indicate that a quantum mechanical treatment of the donor–acceptor vibrational motion is not critical for this proton transfer model. The rates are the same within statistical uncertainty for simulations in which only the hydrogen motion is treated quantum mechanically and simulations in which both the hydrogen and the donor–acceptor vibrational motions are treated quantum mechanically. When the donor–acceptor mode is treated quantum mechanically, the energy splitting between the lowest two vibrational states is smaller out of the coupling region because the excited vibrational state corresponds to excitation of the donor–acceptor mode. On the other hand, the Boltzmann population of the excited vibrational state is relatively small, and nonadiabatic transitions are not dominant out of the coupling region due to small nonadiabatic coupling. Thus, the differences out of the coupling region do not significantly influence the overall rate. In the coupling region, the excited vibrational state corresponds to excitation of the hydrogen vibrational mode for both the classical and the quantum treatment of the donor–acceptor mode. The energy splittings and nonadiabatic couplings, and therefore the quantum amplitudes and the number of nonadiabatic transitions, are similar in the coupling region for both types of simulations.

Reference 36 provides a detailed comparison of rates and kinetic isotope effects for this model system calculated with various approaches, including the Landau–Zener curve-crossing transition state method,⁷ the centroid path integral quantum transition state method,^{7,33} quantum Kramers approaches,^{34,35} and semiclassical variational transition state theory.³⁶ The rate constants vary by over two orders of magnitude for the various approaches. The MDQT rates are in best agreement with the semiclassical variational transition state theory including multidimensional tunneling contributions.³⁶ The present MDQT calculations eliminate the possibility that the classical treatment of the donor–acceptor vibrational mode is the basis for discrepancies between the rates calculated with MDQT and with other methods. Moreover, classically forbidden transitions were shown to be infrequent in the coupling region, and the rates were found to be relatively insensitive to the method of velocity adjustment after such forbidden transitions.

The conclusions of this study are important for future mixed quantum/classical molecular dynamics simulations of proton transfer reactions in solution and enzymes. The donor–acceptor vibrational motion has been shown to play a critical role in such reactions.^{1,2,47} Thus, fundamental insight into the characteristics of this mode is useful for the analysis of data and the development of new algorithms. Note that the quantum treatment of the donor–acceptor vibrational motion may be more important for other systems with varying characteristics, such as different frequencies of this mode or stronger couplings of this mode to other modes in the system. Furthermore, in many reactions the transferring hydrogen nucleus must be represented as a three-dimensional wave function, and in some cases secondary hydrogen nuclei should also be treated quantum mechanically. The calculation of such multidimensional wave functions with grid-

based methodology⁴¹ is computationally expensive. Currently efforts are being directed at alternative approaches for the calculation of multidimensional nuclear wave functions in proton transfer systems.⁴⁸

ACKNOWLEDGMENTS

We thank Kim Wong, Alexander Soudackov, and Bruce Garrett for helpful discussions. We are grateful for financial support from AFOSR Grant No. F49620-01-1-0046, NSF Grant No. CHE-0096357, and NIH Grant No. GM56207.

- ¹D. Borgis and J. T. Hynes, *Chem. Phys.* **170**, 315 (1993).
- ²D. Borgis and J. T. Hynes, *J. Phys. Chem.* **100**, 1118 (1996).
- ³A. Warshel and Z. T. Chu, *J. Chem. Phys.* **93**, 4003 (1990).
- ⁴J. K. Hwang, Z. T. Chu, A. Yadav, and A. Warshel, *J. Phys. Chem.* **95**, 8445 (1991).
- ⁵J. K. Hwang and A. Warshel, *J. Am. Chem. Soc.* **118**, 11745 (1996).
- ⁶D. H. Li and G. A. Voth, *J. Phys. Chem.* **95**, 10425 (1991).
- ⁷H. Azzouz and D. Borgis, *J. Chem. Phys.* **98**, 7361 (1993).
- ⁸R. Pomes and B. Roux, *Chem. Phys. Lett.* **234**, 416 (1995).
- ⁹M. E. Tuckerman, D. Marx, M. L. Klein, and M. Parrinello, *Science* **275**, 817 (1997).
- ¹⁰J. S. Cao and G. A. Voth, *J. Chem. Phys.* **100**, 5093 (1994).
- ¹¹J. S. Cao and G. A. Voth, *J. Chem. Phys.* **100**, 5106 (1994).
- ¹²J. S. Cao and G. A. Voth, *J. Chem. Phys.* **101**, 6157 (1994).
- ¹³J. S. Cao and G. A. Voth, *J. Chem. Phys.* **101**, 6168 (1994).
- ¹⁴D. Borgis, G. Tarjus, and H. Azzouz, *J. Phys. Chem.* **96**, 3188 (1992).
- ¹⁵D. Laria, G. Ciccotti, M. Ferrario, and R. Kapral, *J. Chem. Phys.* **97**, 378 (1992).
- ¹⁶A. Staib, D. Borgis, and J. T. Hynes, *J. Chem. Phys.* **102**, 2487 (1995).
- ¹⁷P. Bala, B. Lesyng, and J. A. McCammon, *Chem. Phys.* **180**, 271 (1994).
- ¹⁸P. Bala, P. Grochowski, B. Lesyng, and J. A. McCammon, *J. Phys. Chem.* **100**, 2535 (1996).
- ¹⁹S. Hammes-Schiffer and J. C. Tully, *J. Chem. Phys.* **101**, 4657 (1994).
- ²⁰S. Hammes-Schiffer, *J. Phys. Chem. A* **102**, 10443 (1998).
- ²¹S. Hammes-Schiffer, in *Advances in Classical Trajectory Methods*, edited by W. L. Hase (JAI, Stamford, 1998), Vol. 3, p. 73.
- ²²C. Alhambra, J. C. Corchado, M. L. Sanchez, J. L. Gao, and D. G. Truhlar, *J. Am. Chem. Soc.* **122**, 8197 (2000).
- ²³C. Alhambra, J. L. Gao, J. C. Corchado, J. Villa, and D. G. Truhlar, *J. Am. Chem. Soc.* **121**, 2253 (1999).
- ²⁴J. Mavri, H. J. C. Berendsen, and W. F. van Gunsteren, *J. Phys. Chem.* **97**, 13469 (1993).
- ²⁵K. Ando and J. T. Hynes, *J. Phys. Chem. B* **101**, 10464 (1997).
- ²⁶D. G. Truhlar, Y.-P. Liu, G. K. Schenter, and B. C. Garrett, *J. Phys. Chem.* **98**, 8396 (1994).
- ²⁷S. R. Billeter, S. P. Webb, T. Iordanov, P. K. Agarwal, and S. Hammes-Schiffer, *J. Chem. Phys.* **114**, 6925 (2001).
- ²⁸D. Borgis, G. Tarjus, and H. Azzouz, *J. Phys. Chem.* **96**, 3188 (1992).
- ²⁹J. C. Tully, *J. Chem. Phys.* **93**, 1061 (1990).
- ³⁰S. R. Billeter, S. P. Webb, P. K. Agarwal, T. Iordanov, and S. Hammes-Schiffer, *J. Am. Chem. Soc.* **123**, 11262 (2001).
- ³¹P. K. Agarwal, S. R. Billeter, and S. Hammes-Schiffer, *J. Phys. Chem. B* **106**, 3283 (2002).
- ³²J. B. Watney, P. K. Agarwal, and S. Hammes-Schiffer, *J. Am. Chem. Soc.* **125**, 3745 (2003).
- ³³H. Azzouz and D. Borgis, *J. Mol. Liq.* **61**, 17 (1994).
- ³⁴D. Antoniou and S. D. Schwartz, *J. Chem. Phys.* **110**, 465 (1999).
- ³⁵D. Antoniou and S. D. Schwartz, *J. Chem. Phys.* **110**, 7359 (1999).
- ³⁶R. P. McRae, G. K. Schenter, B. C. Garrett, Z. Svetlicic, and D. G. Truhlar, *J. Chem. Phys.* **115**, 8460 (2001).
- ³⁷J. Morelli and S. Hammes-Schiffer, *Chem. Phys. Lett.* **269**, 161 (1997).
- ³⁸J.-Y. Fang and S. Hammes-Schiffer, *J. Chem. Phys.* **107**, 8933 (1997).
- ³⁹J. Y. Fang and S. Hammes-Schiffer, *J. Chem. Phys.* **110**, 11166 (1999).
- ⁴⁰C. C. Marston and G. G. Balint-Kurti, *J. Chem. Phys.* **91**, 3571 (1989).
- ⁴¹S. P. Webb and S. Hammes-Schiffer, *J. Chem. Phys.* **113**, 5214 (2000).
- ⁴²E. R. Davidson, *J. Chem. Phys.* **17**, 87 (1975).
- ⁴³H. C. Andersen, *J. Comput. Phys.* **52**, 24 (1983).

- ⁴⁴W. H. Press, B. P. Flannery, S. A. Teukolsky, and W. T. Vetterling, *Numerical Recipes in C* (Cambridge University Press, Cambridge, 1988).
- ⁴⁵U. Muller and G. Stock, J. Chem. Phys. **107**, 6230 (1997).
- ⁴⁶A. W. Jasper, M. D. Hack, and D. G. Truhlar, J. Chem. Phys. **115**, 1804 (2001).
- ⁴⁷M. J. Knapp and J. P. Klinman, Eur. J. Biochem. **269**, 3113 (2002).
- ⁴⁸S. P. Webb, T. Iordanov, and S. Hammes-Schiffer, J. Chem. Phys. **117**, 4106 (2002).